# Space Vector Modulation Strategy for Common-Mode Voltage Suppression in the Reduced Switch Count Three-Level Inverter With Unbalanced Neutral-Point Voltages

Zhiyuan CHU, Changwei QIN, Xiaoyan LI, Jingyang FANG, Lei YANG, and Yanling ZHANG

***Abstract*—The reduced switch count three-level inverter (RSC TLI) has been proposed to save the system cost of the conventional three-level inverter. In some special applications, the RSC TLI should be operated with simultaneous lower common-mode voltage (CMV) and unbalanced neutral-point voltage (NPV) conditions. For this reason, this article further proposes a space vector modulation (SVM) strategy that fulfills the above requirements. First, the basic vectors with low CMV amplitudes are selected, and four basic vectors are employed to synthesize the reference vector and achieve NPV flexible control. The duty cycles of the employed basic vectors are obtained by a novel indirect method, and the appropriate switching sequences are designed to further reduce the current harmonic and keep lower switching losses. Finally, the separate control of capacitor voltages is achieved by using a closed-loop control approach to optimally regulate the duty cycles of different basic vectors. Compared with the conventional strategy, the proposed scheme can reduce the CMV magnitude by half and is applicable to unbalanced NPV conditions. The feasibility and effectiveness are verified by experiments.**

***Index Terms*—Common-mode voltage (CMV) suppression, reduced switch count three-level inverter (RSC TLI), space vector modulation (SVM), unbalanced neutral-point voltages (NPVs).**

## I. Introduction

DUE to the advantages of low output current harmonics, high efficiency, and low switching voltage stress, multi-level inverters are widely used in medium-voltage applications, such as photovoltaic (PV) power generation, energy storage, and motor drives [1], [2]. Among them, the three-level inverter (TLI) has been attracted much attention because of its high reliability and simple structure [3], [4].

The reduced switch count three-level inverter (RSC TLI) only contains ten switches and still maintains the multi-level output waveform. Compared to the commonly-used neutral-point-clamped (NPC) TLI and T-type TLI, the RSC TLI reduces two switches [5]. However, the output states of the RSC TLI cannot exceed two at the same time owing to the coupling effects of the coupled unit and independent unit [6]. Thus, the modulation strategies of NPC TLI and T-type TLI cannot be directly employed in the RSC TLI.

Being similar with the NPC and T-type TLI, the neutral-point voltage (NPV) of the RSC TLI is commonly kept to be balanced [7]. However, in some particular cases, the NPV should be controlled to be unequal [8], [9]. For example, the voltages across two dc-link capacitors in centralized PV inverter are generally regulated to be different for realizing separate maximum power point tracking (MPPT) of PV arrays [10]. In high-power ac drive systems, two rectifiers are used to improve the power rating, but the output voltages of both rectifiers are likely to be unequal [11]. Unfortunately, the output currents will be distorted by unbalanced NPVs. Many scholars have investigated the above issues. An asymmetric strategy for the separate dc links of TLI was introduced in [12]. Zhang et al. presented an improved vector synthesis strategy, but the computational difficulty was increased [13]. To solve this issue, a simplified pulse width modulation (PWM) strategy was proposed in [14], which reduced the computational difficulty. The virtual space vector modulation (VSVM) strategy was demonstrated to be suitable for both balanced and unbalanced NPVs [15]. To improve the system efficiency, two different discontinuous PWM (DPWM) strategies were investigated [16], [17]. For the NPC three-level rectifier, a zero-sequence component injection method was proposed [18]. However, this method cannot be applied to arbitrary unbalanced NPVs and arbitrary power factor conditions at the same time. In order to suppress the leakage current, a DPWM was proposed in [19]. Unfortunately, above methods cannot be directly employed for RSC TLI since this

Manuscript received November 14, 2024; revised January 28, 2025; accepted March 02, 2025. Date of publication June 30, 2025; date of current version April 18, 2025. This work was supported in part by Taishan Scholar Project of Shandong Province under the Grant tsqn202312223, Natural Science Foundation of Shandong Province under the Grant ZR2024MF039, and Development Plan for Youth Innovation Team of Higher Education Institutions in Shandong Province under the Grant 2023KJ127. (*Corresponding author: Changwei Qin, Xiaoyan Li, and Jingyang Fang.*)

Z.Chu, C. Qin, X. Li, L. Yang, and Y. Zhang are with the School of Information and Electrical Engineering and Shandong Key Laboratory of Smart Buildings and Energy Efficiency, Shandong Jianzhu University, Jinan 250101, China (e-mail: 2022085105@stu.sdjzu.edu.cn; qinchangwei20@sdjzu.edu.cn; xylee2023@sdjzu.edu.cn; 2023080103@stu.sdjzu.edu.cn; zhangyanling19@sdjzu.edu.cn).

J. Fang is with the School of Control Science and Engineering, Shandong University, Jinan 250061, China (e-mail: jingyangfang@sdu.edu.cn).

Digital Object Identifier 10.24295/CPSSTPEA.2025.00010

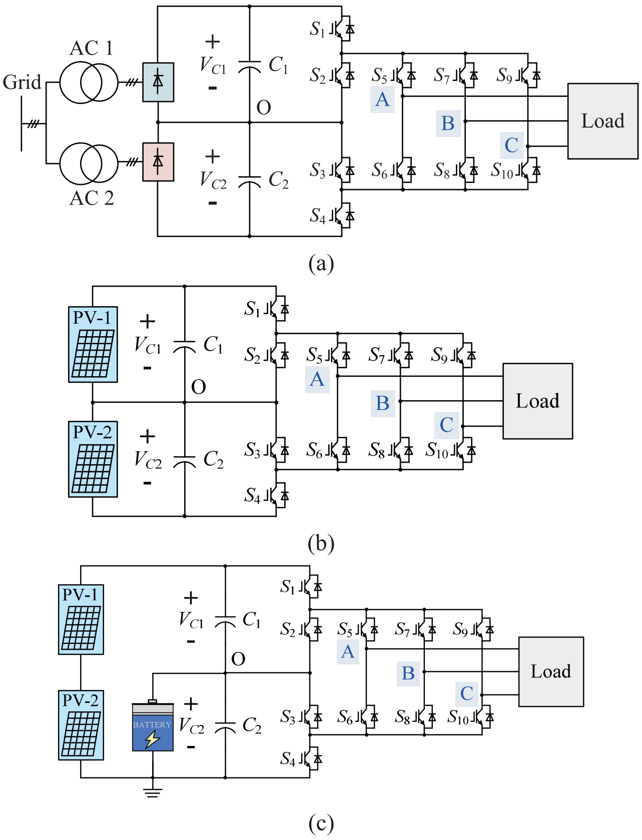


Fig. 1. Three configurations of the RSC TLI with unbalanced NPV conditions. (a) AC drive system. (b) Centralized PV inverter. (c) MPC connected PV–battery hybrid system.

topology is unable to generate medium vectors. For the RSC TLI, an improved virtual SVM (IVSVM) was put forward with unbalanced NPVs, which can enhance the quality of output currents [11]. However, the common-mode voltage (CMV) is very high.

The CMV is generated by the high-frequency action of the switches, which leads to a number of harmful issues. In transformerless PV inverters, the high CMV amplitude triggers the leakage current, which deteriorates the quality of output currents and even threatens the safety of human beings [20]. In motor drive systems, the CMV causes electromagnetic interference (EMI) and generates enormous bearing currents, which decreases the lifetime of the bearings and even damage motors [21].

Presently, the CMV suppression strategies can be categorized into hardware-based and software-based approaches. For hardware-based approaches, the common-mode inductors and common-mode transformers are utilized to suppress the CMV, which however increase the size and volume of the system. Software-based approaches can suppress the CMV only by modifying the modulation strategy, which is a significant benefit. In order to eliminate the CMV of TLI a modulation strategy based on medium and zero vectors was offered in [22], but the dc voltage utilization was decreased. In [23], the large, medium and zero-vector modulation (LMZVM) strategy was presented to reduce the CMV amplitude to one-sixth of dc voltage. Unfortunately, the above two strategies cannot realize active NPV control. Based on [23], a large, medium, small and zero-vector modulation (LMSZVM) strategy was introduced to simultaneously reduce the CMV and control NPV [24]. In [20], a carrier-based PWM (CBPWM) strategy was investigated, which suppressed the CMV with unbalanced NPVs by limiting the range of zero-sequence component. A data-driven strategy for CMV suppression was investigated in [25]. Unfortunately, the strategy requires a large inductor since it is essentially a type of predictive control. An optimal space vector-based hybrid PWM scheme was introduced to simultaneously reduce CMV and line current ripple [26]. However, the output currents of the method are not satisfactory due to discarding the zero vectors [27]. Yan et al. proposed a carrier-based discontinuous SVM (DSVM) method to suppress the CMV [28]. However, this method cannot flexibly regulate the NPV. In addition, a CMV reduction method-based flexible power control was proposed for PV-battery hybrid systems [29].

However, the above modulation strategies are only applicable to the NPC and T-type TLIs. For the RSC TLI, a modulation strategy was suggested in [30], which simultaneously reduced the CMV and controls the NPV balance. However, this method merely considers balanced NPV condition and cannot be applied to unbalanced NPVs.

Aiming at the above-mentioned issues, this article presents a novel SVM strategy for suppressing the CMV in the RSC TLI with unbalanced NPVs. The innovation consists of the following four points.

1) The CMV magnitudes of the basic vectors with unbalanced NPVs are analyzed. The basic vectors with low CMV magnitudes are retained. Meanwhile, this paper reveals the relationship between the basic vectors for the RSC TLI and the dc unbalancing coefficient, and the space vector diagrams (SVD) for different dc unbalancing coefficients are established to suppress the CMV.

2) Based on the established SVD, each sector is further divided into two regions. four basic vectors are optimally selected to synthesize the reference vector in all regions, and a degree of control freedom is provided to flexibly control the capacitor voltages. The duty cycles of the basic vectors are obtained by using an indirect method, and the appropriate switching sequences are designed.

3) The separate control of capacitor voltages is achieved by modifying the duty cycles of the selected basic vectors, and the quality of output currents remains unaffected.

4) In order to validate the feasibility of the presented strategy, extensive experimental tests have been carried out. The obtained results of different modulation indices and dc unbalancing coefficients indicate that the presented strategy can ensure the good waveforms of the output currents. Furthermore, the separate control of capacitor voltages for the proposed strategy can be verified by the short transient process.

This article is outlined as follows: Section II displays the working principle of the RSC TLI with unbalanced NPVs. The proposed modulation strategy is elaborated in Section III. The experimental results are provided in Section IV. Some concluding remarks are given in Section V.

TABLE I
BASIC VECTORS AND CMVS OF THE RSC TLI

| Type | Vectors | CMV | Vectors | CMV |
|---|---|---|---|---|
| Large | [PNN] | $(V_{C1}-2V_{C2})/3$ | [NPP] | $(2V_{C1}-V_{C2})/3$ |
| | [PPN] | $(2V_{C1}-V_{C2})/3$ | [NNP] | $(V_{C1}-2V_{C2})/3$ |
| | [NPN] | $(V_{C1}-2V_{C2})/3$ | [PNP] | $(2V_{C1}-V_{C2})/3$ |
| P-Type Small | [POO] | $V_{C1}/3$ | [PPO] | $2V_{C1}/3$ |
| | [OPO] | $V_{C1}/3$ | [OPP] | $2V_{C1}/3$ |
| | [OOP] | $V_{C1}/3$ | [POP] | $2V_{C1}/3$ |
| N-Type Small | [ONN] | $-2V_{C2}/3$ | [OON] | $-V_{C2}/3$ |
| | [NON] | $-2V_{C2}/3$ | [NOO] | $-V_{C2}/3$ |
| | [NNO] | $-2V_{C2}/3$ | [ONO] | $-V_{C2}/3$ |
| Zero | [PPP] | $V_{C1}$ | [NNN] | $-V_{C2}$ |
| | [OOO] | 0 | | |

## II. WORKING PRINCIPLE OF THE RSC TLI WITH UNBALANCED NPVS

Two different configurations of the RSC TLI with unbalanced NPV conditions are displayed in Fig. 1(a) and (b), in which two PV arrays or rectifiers are used to implement the separate MPPT control or increase the power rating, and the unbalanced NPV conditions occur. Furthermore, the topology of the multiport dc-ac converter (MPC) connected to PV-battery hybrid system is shown in Fig. 1(c). It can be seen that one of the voltage-dividing capacitors of the RSC TLI is connected to the battery as a new dc port, while the original dc-link remains as the other dc port connected to two PV arrays. The unbalanced NPVs can also occur if the voltage across PV array is not equal to the voltage across the battery. Therefore, the starting point of the proposed strategy is reasonable.

In order to make the analysis easier, the dc unbalancing coefficient $\varphi$ is expressed as:

$$\varphi = \frac{V_{C1} - V_{C2}}{V_{C1} + V_{C2}} = \frac{V_{\text{diff}}}{V_{\text{dc}}} \tag{1}$$

where $V_{C1}$ and $V_{C2}$ are the voltages across capacitors $C_1$ and $C_2$, respectively. $V_{\text{diff}}$ is the voltage difference across $C_1$ and $C_2$. $V_{\text{dc}}$ is the total dc-link voltage.

It can be seen that the dc $\varphi$ ranges from $-1$ to 1. From (1), $V_{C1}$ and $V_{C2}$ can be expressed as:

$$\begin{cases} V_{C1} = \dfrac{1+\varphi}{2} V_{\text{dc}} \\ V_{C2} = \dfrac{1-\varphi}{2} V_{\text{dc}} \end{cases} \tag{2}$$

Being similar with the conventional NPC and T-type TLI, the RSC TLI has three output voltage states, as, P, O, and N. Choosing the neutral-point (O) as the reference, the corresponding output voltages are $V_{C1}$, 0, and $-V_{C2}$, respectively.

The CMV is represented by $v_{\text{cm}}$, which is defined as the average value of three-phase output voltages $v_{\text{ao}}$, $v_{\text{bo}}$, and $v_{\text{co}}$ [20], as expressed by (3).

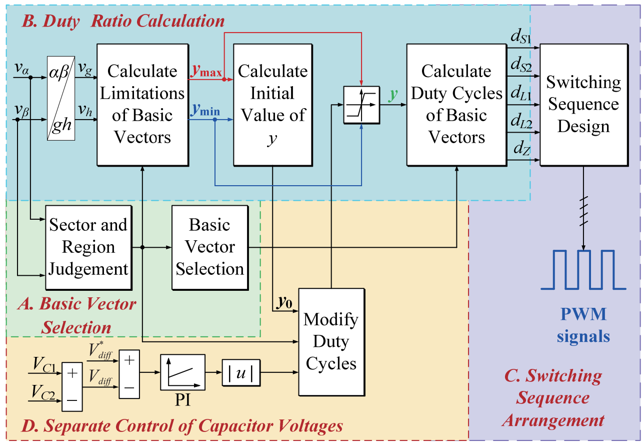


Fig. 2. Control diagram of the proposed strategy.

$$v_{\text{cm}} = \frac{v_{\text{ao}} + v_{\text{bo}} + v_{\text{co}}}{3} \tag{3}$$

Limited by the circuit constraints, the medium vectors in conventional NPC or T-type TLIs cannot be generated, and the conventional SVM strategy cannot be directly applied in the RSC TLI [6]. With the unbalanced NPV conditions, Table I summarizes the CMV of the basic vectors, which are calculated based on (3). It is easy to see that the CMV magnitudes are relatively high for basic vectors in red color. Therefore, the CMV can be suppressed by discarding the basic vectors marked in red color, while the remaining vectors are used to synthesize the reference vector. Based on this principle, the proposed SVM strategy for CMV suppression will be elaborated in the next section.

## III. PROPOSED SVM STRATEGY FOR CMV SUPPRESSION

The proposed SVM strategy for CMV suppression in the RSC TLI with unbalanced NPVs includes four parts. Fig. 2 shows the control diagram of the proposed strategy. In part A, the basic vector selection is introduced to suppress the CMV. The duty cycle calculation of the basic vectors is presented in part B. In part C, the switching sequence is properly arranged. Finally, the separate control of capacitor voltages is achieved by using a closed-loop control approach to optimally regulate the duty cycles of different basic vectors.

### *A. Basic Vector Selection*

Based on the CMV analysis above, Fig. 3 shows the SVD with different DC unbalancing coefficients ($\varphi$) of the proposed SVM strategy. The amplitude of small vectors will be affected by the dc unbalancing coefficient, and the large and zero vectors are not affected. The SVD is divided into 6 sectors, and each sector is further divided into two regions (regions A and B).

Taking sector I as an example, the sector contains small vector $V_{S1}$ [POO], small vector $V_{S2}$ [OON], large vector $V_{L1}$ [PNN], large vector $V_{L2}$ [PPN], and zero vector $V_Z$ [OOO], which are expressed as:

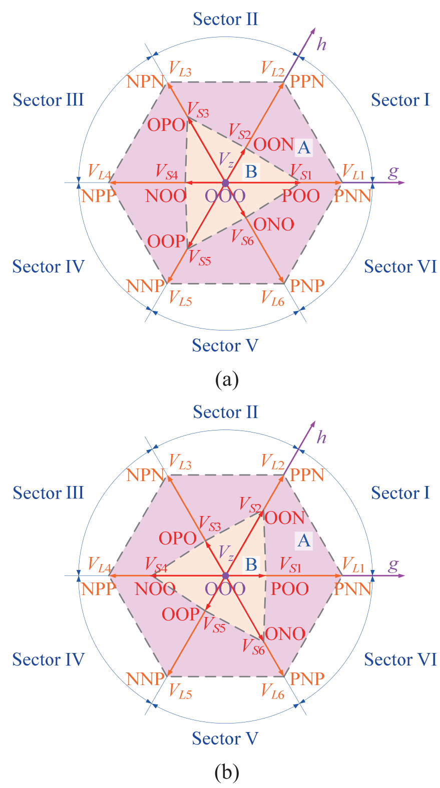


Fig. 3. SVD of the proposed strategy. (a) $\varphi > 0$. (b) $\varphi < 0$.

$$\begin{cases} V_{S1} = \dfrac{1+\varphi}{3} V_{dc} \cdot e^{j0} \\ V_{S2} = \dfrac{1-\varphi}{3} V_{dc} \cdot e^{j\frac{\pi}{3}} \\ V_{L1} = \dfrac{2}{3} V_{dc} \cdot e^{j0} \\ V_{L2} = \dfrac{2}{3} V_{dc} \cdot e^{j\frac{\pi}{3}} \\ V_{Z} = 0 \end{cases} \tag{4}$$

When the reference vector locates in region A, four nearest basic vectors are used to synthesize the reference vector. Since both P-type and N-type small vectors are contained in this region, the NPV can be flexibly controlled. While for region B, the basic vector generally selected according to the nearest three-vector principle, which cannot realize the separate control of capacitor voltages. To cope with the difficulty, a large vector is added, which means that four vectors are adopted to synthesize the reference vector. In this way, a novel control degree of freedom can be generated, and the NPV control can be achieved. Table II shows the basic vector selection for different regions of each sector.

### *B. Duty Ratio Calculation*

To simplify the calculation, the 60° coordinate system is employed. $v_g$ and $v_h$ are the $g$-axis and $h$-axis components, which can be expressed as:

TABLE II
THE BASIC VECTOR SELECTION IN DIFFERENT SECTORS

| Sector | Region A | Region B |
|---|---|---|
| I | [POO], [OON], [PNN], [PPN] | [OOO], [POO], [OON], [PNN] or [PPN] |
| II | [OON], [OPO], [PPN], [NPN], | [OOO], [OON], [OPO], [PPN] or [NPN] |
| III | [OPO], [NOO], [NPN], [NPP] | [OOO], [OPO], [NOO], [NPN] or [NPP] |
| IV | [NOO], [OOP], [NPP], [NNP] | [OOO], [NOO], [OOP], [NPP] or [NNP] |
| V | [OOP], [ONO], [NNP], [PNP] | [OOO], [OOP], [ONO], [NNP] or [PNP] |
| VI | [ONO], [POO], [PNP], [PNN] | [OOO], [ONO], [POO], [PNP] or [PNN] |

$$\begin{cases} v_g = v_\alpha - \dfrac{\sqrt{3}}{3} v_\beta \\ v_h = \dfrac{2\sqrt{3}}{3} v_\beta \end{cases} \tag{5}$$

where $v_\alpha$ and $v_\beta$ are two components of reference vector in orthogonal coordinate system. The duty ratio calculation in regions A and B are analyzed as follows:

1) Region A of Sector I: In this region, four basic vectors are selected to synthesize reference vector, and the volt-second balance equation is written as follows:

$$\begin{cases} V_{S1} \cdot d_{S1} + V_{S2} \cdot d_{S2} + V_{L1} \cdot d_{L1} + V_{L2} \cdot d_{L2} = V_{ref} \\ d_{S1} + d_{S2} + d_{L1} + d_{L2} = 1 \end{cases} \tag{6}$$

where $d_{S1}$, $d_{S2}$, $d_{L1}$ and $d_{L2}$ are the duty cycles of $V_{S1}$, $V_{S2}$, $V_{L1}$ and $V_{L2}$, respectively. $V_{ref}$ is the reference vector. (6) is further simplified by substituting (4) into (6) as follows:

$$\begin{cases} \dfrac{1+\varphi}{3} \cdot V_{dc} \cdot d_{S1} + \dfrac{2}{3} \cdot V_{dc} \cdot d_{L1} = v_g \\ \dfrac{1-\varphi}{3} \cdot V_{dc} \cdot d_{S2} + \dfrac{2}{3} \cdot V_{dc} \cdot d_{L2} = v_h \\ d_{S1} + d_{S2} + d_{L1} + d_{L2} = 1 \end{cases} \tag{7}$$

It is worthwhile to start by assuming that the duty cycle of the P-type small vector $d_{S1}$ is a known quantity, whose value is $y$, and the corresponding detailed solution is given in subsection D. On this assumption, $d_{S2}$, $d_{L1}$ and $d_{L2}$ can be obtained:

$$\begin{cases} d_{S2} = \dfrac{1}{1+\varphi} \cdot \dfrac{2V_{dc} - 3v_g - 3v_h}{V_{dc}} - \dfrac{1-\varphi}{1+\varphi} \cdot y \\ d_{L1} = \dfrac{3}{2} \cdot \dfrac{v_g}{V_{dc}} - \dfrac{1+\varphi}{2} \cdot y \\ d_{L2} = \dfrac{1}{2} \cdot \left[ \dfrac{3v_h}{V_{dc}} - \dfrac{1-\varphi}{1+\varphi} \cdot \dfrac{2V_{dc} - 3v_g - 3v_h}{V_{dc}} + \dfrac{(1-\varphi)^2}{1+\varphi} \cdot y \right] \end{cases} \tag{8}$$

As the duty cycles of each basic vector take values between 0 and 1, the range of $y$ can be expressed as:

$$\begin{cases} y < \dfrac{1}{1-\varphi} \cdot \dfrac{2V_{dc} - 3v_g - 3v_h}{V_{dc}} \cdot \dfrac{1}{1+\varphi} \cdot \dfrac{3v_g}{V_{dc}} \\ y < \dfrac{1}{1+\varphi} \cdot \dfrac{3v_g}{V_{dc}} \\ y > \dfrac{1}{1-\varphi} \cdot \dfrac{2V_{dc} - 3v_g - 3v_h}{V_{dc}} - \dfrac{1+\varphi}{(1-\varphi)^2} \cdot \dfrac{3v_h}{V_{dc}} \end{cases} \tag{9}$$

Thus, the maximum value ($y_{max}$) and minimum value ($y_{min}$) of $y$ are given in (10) and (11), respectively.

$$y_{max} = \min\left\{ 1, \frac{1}{1-\varphi} \cdot \frac{2V_{dc} - 3v_g - 3v_h}{V_{dc}}, \frac{1}{1+\varphi} \cdot \frac{3v_g}{V_{dc}} \right\} \tag{10}$$

$$y_{min} = \max\left\{ 0, \frac{1}{1-\varphi} \cdot \frac{2V_{dc} - 3v_g - 3v_h}{V_{dc}} - \frac{1+\varphi}{(1-\varphi)^2} \cdot \frac{3v_h}{V_{dc}} \right\} \tag{11}$$

For convenient calculation, the initial value of $y$ ($y_0$) is taken as the arithmetic mean of its maximum and minimum values, as shown in (12).

$$y_0 = \frac{y_{max} + y_{min}}{2} \tag{12}$$

By substituting (12) into (8), the duty cycles of other basic vectors can be derived.

2) Region B of Sector I: In this region, the NPV can be flexibly controlled by adding a large vector to synthesize the reference vector, which is classified into two cases according to the difference between the reference value of voltage difference across $C_1$ and $C_2$ ($V^*_{diff}$) and $V_{diff}$.

Case 1: If $V^*_{diff} \leqslant V_{diff}$, four basic vectors [OOO], [POO], [OON], and [PPN] are adopted to synthesize the reference vector. In this case, the volt-second balance equation is as follows:

$$\begin{cases} V_Z \cdot d_Z + V_{S1} \cdot d_{S1} + V_{S2} \cdot d_{S2} + V_{L2} \cdot d_{L2} = V_{ref} \\ d_Z + d_{S1} + d_{S2} + d_{L2} = 1 \end{cases} \tag{13}$$

where $V_Z$ denotes [OOO]. $d_Z$ is the duty cycle of $V_Z$.

If the duty cycle $d_{L2}$ of the large vector is considered as a known quantity $y$, the above equations can be expressed as:

$$\begin{cases} d_{L2} = y \\ d_{S1} = \dfrac{1}{1+\varphi} \cdot \dfrac{3v_g}{V_{dc}} \\ d_{S2} = \dfrac{1}{1-\varphi} \cdot \left( \dfrac{3v_h}{V_{dc}} - 2y \right) \\ d_Z = 1 - y - \dfrac{1}{1+\varphi} \cdot \dfrac{3v_g}{V_{dc}} - \dfrac{1}{1-\varphi} \cdot \left( \dfrac{3v_h}{V_{dc}} - 2y \right) \end{cases} \tag{14}$$

It can be seen that $d_{S1}$ is not related to $d_{L2}$, but $d_{S2}$ will be decreased by increasing $d_{L2}$. It is known that the P-type small vector decreases the voltage across $C_1$ and increase the voltage across $C_2$. The N-type small vector has the opposite effects.

TABLE III
SWITCHING STATES OF ZERO VECTORS FOR THE RSC TLI

| Vectors | ON switches | Vectors | ON switches |
|---|---|---|---|
| $[OOO]_{-1}$ | {2, 3, 5, 8, 10} | $[OOO]_{-2}$ | {2, 3, 5, 7, 10} |
| $[OOO]_{-3}$ | {2, 3, 6, 7, 10} | $[OOO]_{-4}$ | {2, 3, 6, 7, 9} |
| $[OOO]_{-5}$ | {2, 3, 6, 8, 9} | $[OOO]_{-6}$ | {2, 3, 5, 8, 9} |

Consequently, increasing the duty cycle of the large vector will reduce the difference between $V^*_{diff}$ and $V_{diff}$.

By restricting the duty cycle of the basic vectors, $y_{max}$ and $y_{min}$ are denoted as (15) and (16), respectively.

$$y_{min} = \max\left\{ 0, \frac{1-\varphi}{(1+\varphi)^2} \cdot \frac{3v_g}{V_{dc}} + \frac{1}{1+\varphi} \cdot \frac{3v_h}{V_{dc}} - \frac{1-\varphi}{1+\varphi} \right\} \tag{15}$$

$$y_{max} = \min\left\{ 1, \frac{1}{2} \cdot \frac{3v_h}{V_{dc}} \right\} \tag{16}$$

Case 2: When $V^*_{diff} > V_{diff}$, [OOO], [POO], [OON], and [PNN] are adopted to synthesize the reference vector. The duty cycles of basic vectors can be expressed as:

$$\begin{cases} d_{L1} = y \\ d_{S1} = \dfrac{1}{1+\varphi} \cdot \left( \dfrac{3v_g}{V_{dc}} - 2y \right) \\ d_{S2} = \dfrac{1}{1-\varphi} \cdot \dfrac{3v_h}{V_{dc}} \\ d_Z = 1 - y - \dfrac{1}{1-\varphi} \cdot \dfrac{3v_h}{V_{dc}} - \dfrac{1}{1+\varphi} \cdot \left( \dfrac{3v_g}{V_{dc}} - 2y \right) \end{cases} \tag{17}$$

Similarly, $y_{max}$ and $y_{min}$ can be denoted as follows:

$$y_{min} = \max\left\{ 0, \frac{1+\varphi}{(1-\varphi)^2} \cdot \frac{3v_h}{V_{dc}} + \frac{1}{1-\varphi} \cdot \frac{3v_g}{V_{dc}} - \frac{1+\varphi}{1-\varphi} \right\} \tag{18}$$

$$y_{max} = \min\left\{ 1, \frac{3v_g}{2V_{dc}} \right\} \tag{19}$$

The value of $y$ is obtained from the output of proportional-integral (PI) regulator, whose steps will be given Subsection D. The duty cycles of each basic vector can be obtained by substituting the obtained $y$ into (14) or (17).

### C. Switching Sequence Design

In order to reduce the harmonics of output currents and to keep lower switching losses, the appropriate switching sequences for different cases are carefully designed. It should be noted that the zero vector [OOO] contains six redundant states, so different states should be selected for different sectors. Table III displays the zero vectors with low CMV magnitudes and the corresponding switching states.

To further reduce the harmonics of the output currents, the switching sequences are arranged symmetrically on both sides.

TABLE IV
SWITCHING SEQUENCES IN DIFFERENT SECTORS

| Sector | Region | Switching sequence |
|---|---|---|
| I | A | [OON]–[PPN]–[PNN]–[POO]–… |
| | B ($V^*_{\rm diff} \leqslant V_{\rm diff}$) | [OON]–[PPN]–[POO]–[OOO]$_{-1}$–… |
| | B ($V^*_{\rm diff} > V_{\rm diff}$) | [OON]–[OOO]$_{-1}$–[POO]–[PNN]–… |
| II | A | [OON]–[PPN]–[NPN]–[POO]–… |
| | B ($V^*_{\rm diff} \leqslant V_{\rm diff}$) | [OON]–[PPN]–[OPO]–[OOO]$_{-3}$–… |
| | B ($V^*_{\rm diff} > V_{\rm diff}$) | [OON]–[OOO]$_{-3}$–[OPO]–[NPN]–… |
| III | A | [NOO]–[NPP]–[NPN]–[OPO]–… |
| | B ($V^*_{\rm diff} \leqslant V_{\rm diff}$) | [NOO]–[NPP]–[OPO]–[OOO]$_{-3}$–… |
| | B ($V^*_{\rm diff} > V_{\rm diff}$) | [NOO]–[OOO]$_{-3}$–[OPO]–[NNP]–… |
| IV | A | [NOO]–[NPP]–[NNP]–[OOP]–… |
| | B ($V^*_{\rm diff} \leqslant V_{\rm diff}$) | [NOO]–[NPP]–[OOP]–[OOO]$_{-5}$–… |
| | B ($V^*_{\rm diff} > V_{\rm diff}$) | [NOO]–[OOO]$_{-5}$–[OOP]–[NNP]–… |
| V | A | [ONO]–[PNP]–[NNP]–[OOP]–… |
| | B ($V^*_{\rm diff} \leqslant V_{\rm diff}$) | [ONO]–[PNP]–[OOP]–[OOO]$_{-5}$–… |
| | B ($V^*_{\rm diff} > V_{\rm diff}$) | [ONO]–[OOO]$_{-5}$–[OOP]–[NNP]–… |
| VI | A | [ONO]–[PNP]–[PNN]–[POO]–… |
| | B ($V^*_{\rm diff} \leqslant V_{\rm diff}$) | [ONO]–[PNP]–[POO]–[OOO]$_{-1}$–… |
| | B ($V^*_{\rm diff} > V_{\rm diff}$) | [ONO]–[OOO]$_{-1}$–[POO]–[PNN] –… |

For simplicity, the former half of the switching sequences of different sectors are provided in Table IV.

The switching sequence in region A of sector I is designed as: [OON]–[PPN]–[PNN]–[POO]–[PNN]–[PPN]–[OON]. Region A contains both the P-type small vector and the N-type small vector, and the capacitor voltages can be controlled independently, so one sequence is used. Region B is only able to select different large vectors [PNN] or [PPN] according to different NPVs, thus two switching sequences are needed to realize separate control of capacitor voltages. Moreover, all switching sequences are initiated and terminated by the N-type small vector.

## *D. Separate Control of Capacitor Voltages*

To realize the separate control of capacitor voltages, a PI regulator is employed. To be specifics, the difference between $V^*_{\rm diff}$ and $V_{\rm diff}$ is fed to the PI regulator. The absolute value of its output ($y_{\rm np}$) is used to modify the duty cycle of the basic vectors, which can be expressed as:

$$y_{\rm np} = \left| \left( k_{\rm p} + \frac{k_{\rm i}}{s} \right) \cdot \left( V^*_{\rm diff} - V_{\rm diff} \right) \right| \tag{20}$$

where $k_{\rm p}$ and $k_{\rm i}$ are the parameters of the PI regulator.

The separate control of capacitor voltages is available in three cases, which are indicated as follows:

Case 1: When the reference vector is located in the region A and $V^*_{\rm diff} \leqslant V_{\rm diff}$, the duty cycle of the P-type small vector should be increased, so $y$ is modified as:

$$y = y_0 + y_{\rm np} \tag{21}$$

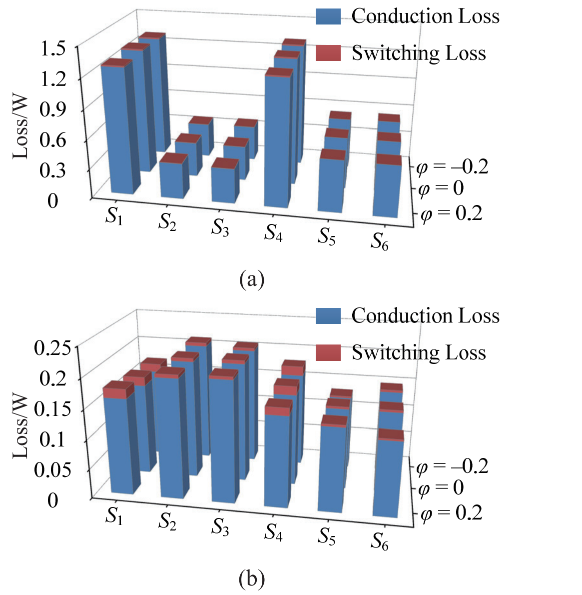


Fig. 4. Losses of power switches for the RSC TLI. (a) $m = 0.8$. (b) $m = 0.4$.

Case 2: When the reference vector is located in the region A and $V^*_{\rm diff} > V_{\rm diff}$, the duty cycle of the P-type small vector should be decreased, so $y$ is modified as:

$$y = y_0 - y_{\rm np} \tag{22}$$

Case 3: When the reference vector is located in the region B, it is sufficient to set the duty cycle of the large vector directly to be $y_{\rm np}$ for easy calculation, which is expressed as:

$$y = y_{\rm np} \tag{23}$$

In addition, the modified duty cycle of the basic vectors should satisfy the above limitations, as expressed by (24).

$$y_{\min} < y < y_{\max} \tag{24}$$

## *E. Loss Analyses of Power Switches*

Since the topology of the RSC TLI is symmetrical, the voltage stress and loss of $S_5$ is identical to those of $S_7$ and $S_9$, and the same conclusion can be obtained for other switches. Therefore, it is sufficient to analyze only power switches $S_1$–$S_6$. In addition, the losses of power switches can be categorized into switching losses and conduction losses.

To visually demonstrate the losses of the proposed strategy, Fig. 4 shows the losses of the proposed strategy for the RSC TLI, which is obtained via PLECS Blockset and MATLAB/Simulink. It can be seen that the losses of power switches are mainly conduction losses and switching losses are very small. When $\varphi = 0.2$, the losses of $S_1$, $S_2$, and $S_5$ are slightly greater than those of $S_4$, $S_3$, and $S_6$. On the contrary, when $\varphi = -0.2$, the losses of $S_1$, $S_2$, and $S_5$ are slightly smaller than those of $S_4$, $S_3$, and $S_6$, respectively. As $m$ is increased, the losses of the power switches are increased correspondingly, because the magnitude of output current is increased.

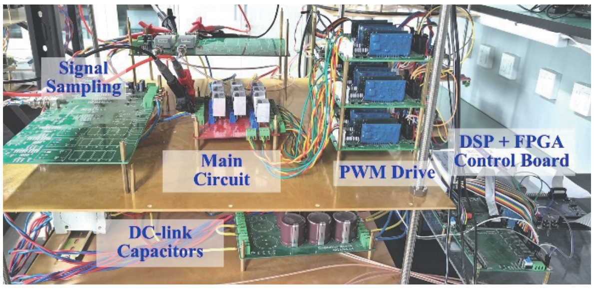


Fig. 5. Photograph of the experimental test rig.

TABLE V
Parameters for the Experimental Tests

| Parameters | Values |
|---|---|
| DC-link voltage ($V_{dc}$) | 100 V |
| DC-link capacitors ($C_1$ and $C_2$) | 1410 μF |
| Fundamental frequency ($f$) | 50 Hz |
| Switching frequency ($f_{sw}$) | 12.5 kHz |
| Sampling period ($T_s$) | 80 μs |
| Dead-time ($t_d$) | 2 μs |
| Resistive-inductive ($RL$) load | 10 Ω, 7 mH |

## IV. Experimental Results

A hardware-based RSC-TLI test rig is designed and built to verify the validity of proposed strategy, as depicted in Fig. 5. Three-phase output voltages are measured, and CMV is obtained by using (3). The digital signal processor TMS320F28335 and field programmable gate array XC3S500E are adopted as controllers. One dc source is adopted as the dc power supply to verify the feasibility and correctness of the separate control of capacitor voltages in this article [16], [31].

The measurements of CMV waveforms experimentally are conducted, and the digital storage oscilloscope RTO2014 from Rohde & Schwarz is further utilized, which can support the mathematical calculation in (3). To be specific, three-phase pole voltages ($v_{ao}$, $v_{bo}$, and $v_{co}$) are measured, and the CMV waveform is obtained by the MATH function in RTO2014. The rest of the photos were captured via the oscilloscope MDO3024 from Tektronix.

In order to effectively demonstrate the advantages of the proposed SVM strategy, the methods in [11] and [30] are used for comparisons. For the convenience of the following description, the method in [11], the method in [30], and the proposed SVM strategy are denoted as Method-1, Method-2, and Method-3, respectively. The parameters for the experimental tests are presented in Table V.

### A. Experimental Results in Steady State

In order to investigate the operating performance in regions A and B of each sector, two modulation indices are chosen, which include 0.8 and 0.4. When $V^*_{\text{diff}}$ is equal to 20 V, the experimental results are shown in Fig. 6.

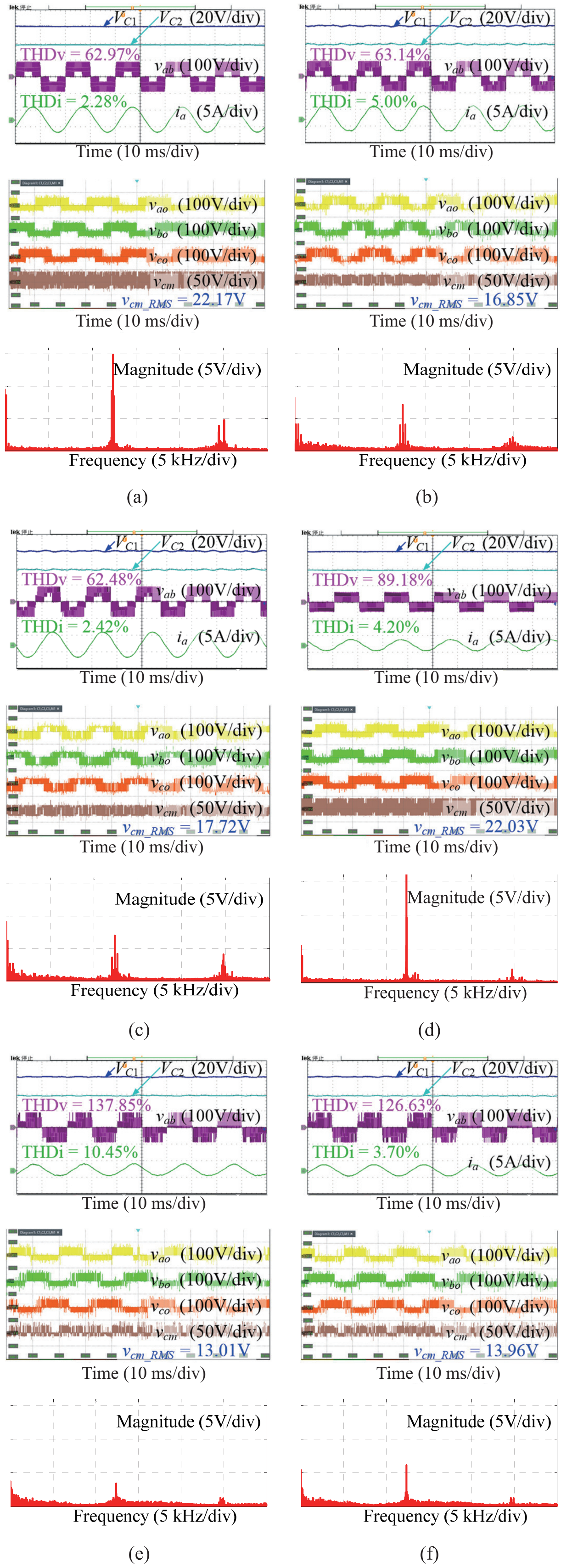


Fig. 6. Experimental results for positive unbalancing coefficient ($\varphi$ = 0.2). (a) Method-1, $m$ = 0.8. (b) Method-2, $m$ = 0.8. (c) Method-3, $m$ = 0.8. (d) Method-1, $m$ = 0.4. (e) Method-2, $m$ = 0.4. (f) Method-3, $m$ = 0.4.

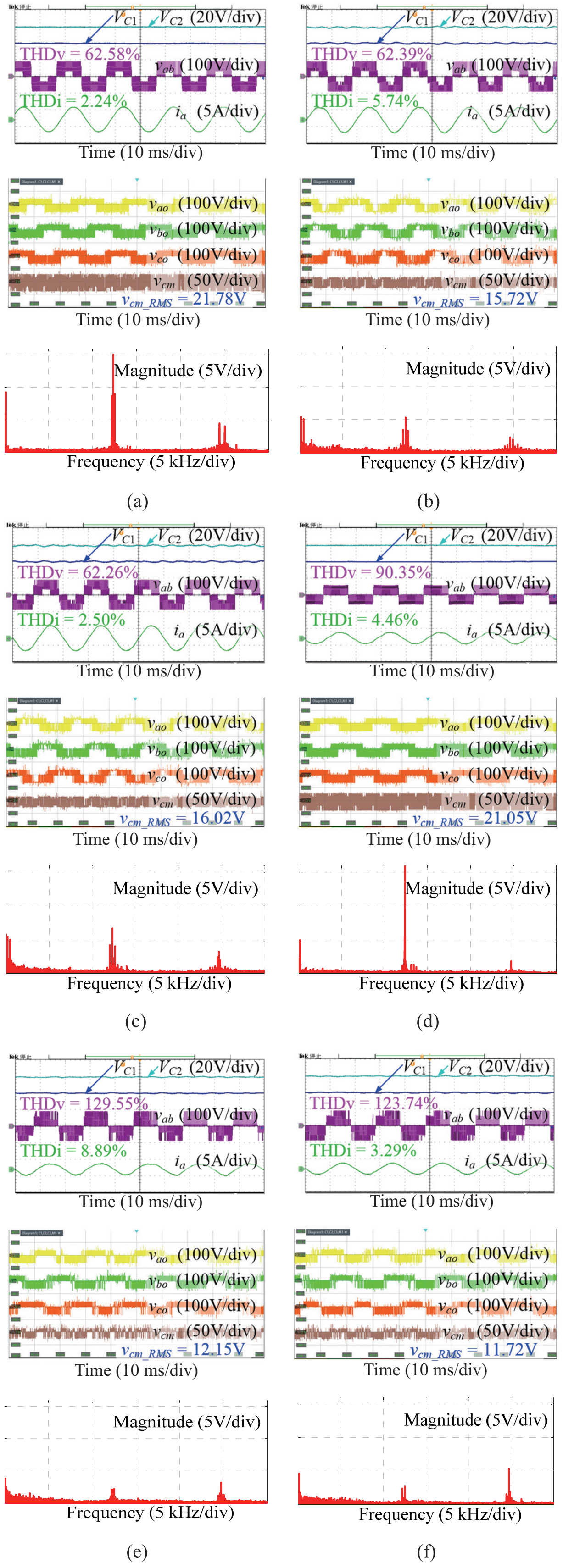


Fig. 7. Experimental results for negative unbalancing coefficient ($\varphi$ = –0.2). (a) Method-1, $m$ = 0.8. (b) Method-2, $m$ = 0.8. (c) Method-3, $m$ = 0.8. (d) Method-1, $m$ = 0.4. (e) Method-2, $m$ = 0.4. (f) Method-3, $m$ = 0.4.

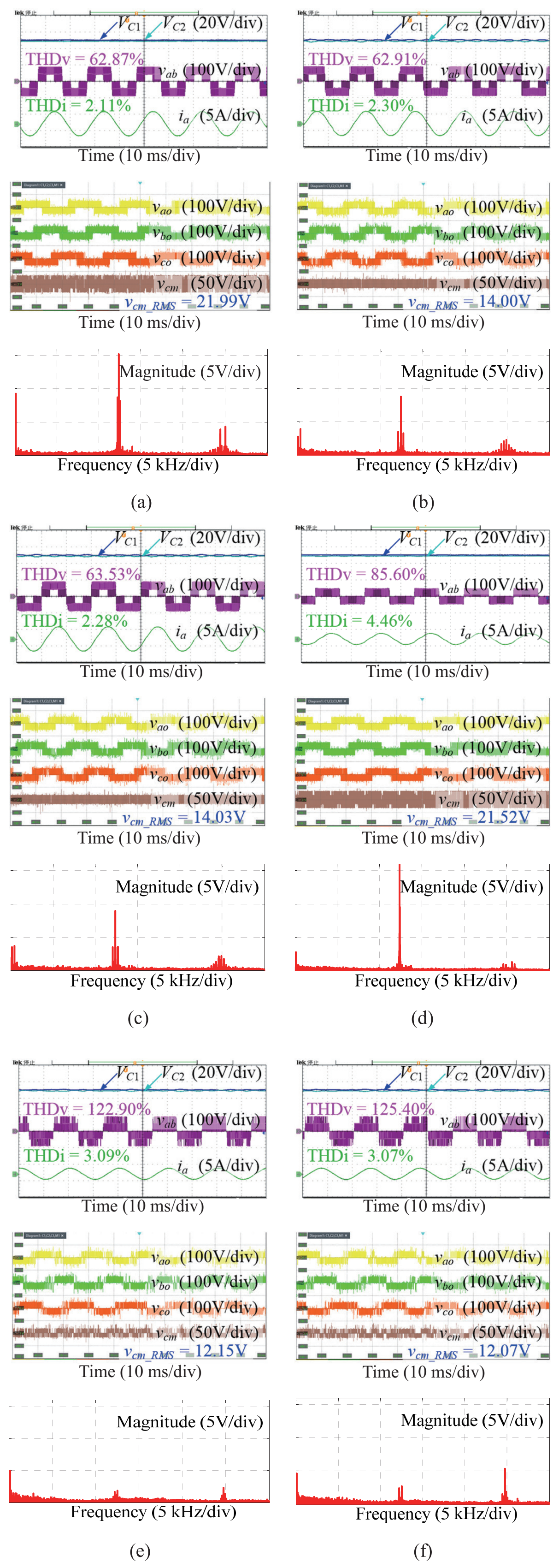


Fig. 8. Experimental results with balanced NPV condition ($\varphi$ = 0). (a) Method-1, $m$ = 0.8. (b) Method-2, $m$ = 0.8. (c) Method-3, $m$ = 0.8. (d) Method-1, $m$ = 0.4. (e) Method-2, $m$ = 0.4. (f) Method-3, $m$ = 0.4.

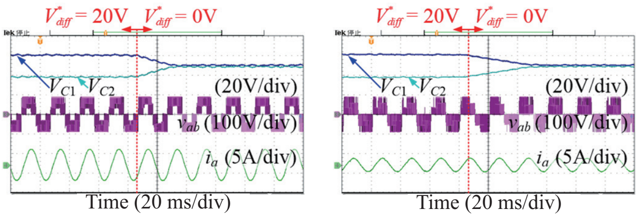


(a) (b)

Fig. 9. Dynamic experimental waveforms from positive dc unbalancing coefficient to balanced NPV condition for Method-3. (a) $m = 0.8$. (b) $m = 0.4$.

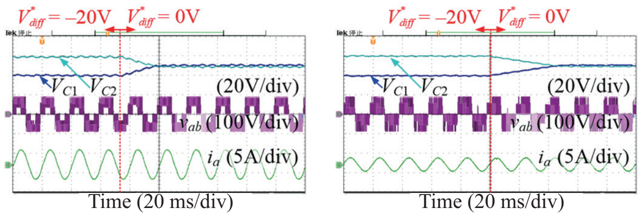


(a) (b)

Fig. 10. Dynamic experimental waveforms from negative dc unbalancing coefficient to balanced NPV condition for Method-3. (a) $m = 0.8$. (b) $m = 0.4$.

Fig. 6(a) − (c) shows the experimental waveforms when the modulation index $m = 0.8$. The line voltages for three methods are five levels. The total harmonic distortion (THD) of output current (THDi) for Method-1 is the minimum, whose value is 2.28%. However, Method-1 synthesizes the reference vector by using all basic vectors, which has the root-mean-square (RMS) value of CMV as high as 22.17 V. Although Method-2 can suppress the CMV, the quality of output currents is obviously degraded, whose THDi is high as 5.00%. Compared to Method-1, the CMV amplitude for Method-3 is reduced by half. Compared with Method-2, the THDi for Method-3 is reduced to 2.42%, and the quality of output currents is significantly improved. Thus, Method-3 can suppress the CMV while ensuring high quality of output currents.

Fig. 6(d) − (f) shows the experimental waveforms when $m = 0.4$. Being similar to the previous results, the RMS values of the CMV are reduced by 40.94% and 36.63% for Method-2 and Method-3, when comparing with Method-1, respectively. In contrast to $m = 0.4$, the quality of output currents for Method-3 is significantly better than that of Method-1, whose THDi is equal to 3.70%.

When $V^*_{\text{diff}}$ is equal to −20 V, the experimental results are shown in Fig. 7. Same as when $\varphi = 0.2$, Method-1 has the highest CMV. Method-2 can suppress the CMV. However, the output currents are distorted. Method-3 can suppress the CMV while maintaining the well quality of output currents.

When $\varphi = 0$, the experimental results are displayed in Fig. 8. The CMV for Method-1 are still the highest. There is almost no difference in the overall performance of Method-2 and Method-3. Therefore, the proposed modulation strategy is also applicable to the condition with balanced NPVs.

The spectra of the CMV are gained by using MATLAB to better analyze the CMV performance, which are offered in Figs. 6 − 8, respectively. The major components of CMV for Method-3 are reduced at different frequencies compared to Method-1. In conclusion, all the results confirm CMV suppression properties of the proposed modulation strategy.

### *B. Dynamic Experimental Results*

When $V^*_{\text{diff}}$ is manually changed, the experimental results for Method-3 are illustrated in Figs. 9 and 10. It can be clearly seen that Method-3 is able to regulate $V_{C1}$ and $V_{C2}$ separately. Moreover, satisfactory waveforms of output currents are guaranteed with balanced and unbalanced NPV conditions.

## V. Conclusion

In this article, a novel SVM strategy for CMV suppression in the RSC TLI with unbalanced NPVs was proposed. The basic vectors with low CMV magnitudes were chosen, which suppressed the CMV. Based on SVD with unbalanced NPVs, four basic vectors were selected to synthesize the reference vector. The duty cycles of basic vectors were calculated by using an indirect method, and the appropriate switching sequences were designed. By modifying the duty cycle of basic vectors, the separate control of capacitor voltages was accomplished. The CMV magnitudes were decreased by half in comparison with the conventional modulation strategy. What's more, the proposed SVM strategy was simultaneously applicable to balanced and unbalanced NPV conditions. The effectiveness of the proposed method was verified by experiments.

It is reported that, the technology in this article is still at the theoretical research stage presently, and the equipment for industrialization is not available. For the industrial equipment based on centralized TLI, the similar modulation strategy that is suitable for both balanced and unbalanced NPVs can be implemented via the digital controller. Doing so, when some non-ideal factors result in unbalanced NPV conditions, the quality of output currents will not be negatively affected.

## References


[1] H. Kanakri, E. C. D. Santos, and M. Rizkalla, "Twelve-step voltage source inverter: a three-phase six-levels inverter using planar transformers," in *CPSS Transactions on Power Electronics and Applications,* vol. 9, no. 1, pp. 263–273, Sept. 2024.

[2] Y. Yang, J. Pan, H. Wen, M. Fan, R. Chen, L. He, M. Xie, M. Norambuena, L. Xu, and J. Rodriguez, "Model predictive current control with low complexity for single-phase four-level hybrid-clamped converters," in *IEEE Transactions on Transportation Electrification,* vol. 7, no. 3, pp. 983–999, Sept. 2021.

[3] J. Chen, D. Jiang, and Q. Li, "Attenuation of conducted EMI for three-level inverters through PWM," in *CPSS Transactions on Power Electronics and Applications,* vol. 3, no. 2, pp. 134–145, Jun. 2018.

[4] Z. Dong, C. Wang, and Q. Cheng, "A hybrid modulation method with the maximum controllable range of the neutral-point current for three-level NPC," in *IEEE Transactions on Transportation Electrification,* vol. 8, no. 4, pp. 4444–4455, Dec. 2022.

[5] X. Xing, M. Jing, C. Du, C. Qin, C. Liu, and Z. Chen, "An adaptive model predictive control for reduced switch count three-level inverter," in *IEEE Journal of Emerging and Selected Topics in Power Electronics,* vol. 11, no. 1, pp. 453–464, Feb. 2023.

[6] C. Qin, X. Xing, and Y. Jiang, "Topology and space vector modulation method for the reduced switch count quasi-Z-source three-level inverter,"

in *IEEE Transactions on Industrial Electronics,* vol. 70, no. 5, pp. 4332–4344, May 2023.

[7] C. Wang, Z. Li, X. Si, and H. Xin, "Control of neutral-point voltage in three-phase four-wire three-level NPC inverter based on the disassembly of zero level," in *CPSS Transactions on Power Electronics and Applications,* vol. 3, no. 3, pp. 213–222, Sept. 2018.

[8] Y. Zou, Y. Xing, L. Zhang, Z. Zheng, X. Liu, H. Hu, T. Wang, and Y. Wang, "Dynamic-space-vector discontinuous PWM for three-phase Vienna rectifiers with unbalanced neutral-point voltage," in *IEEE Transactions on Power Electronics,* vol. 36, no. 8, pp. 9015–9026, Aug. 2021.

[9] Z. Zhang, B. Li, G. Zhang, G. Wang, Z. Huang, B. Hu, T. Long, and D. Xu, "Optimized carrier-based DPWM strategy adopting self-adjusted redundant clamping modes for Vienna rectifiers with unbalanced dc links," in *IEEE Transactions on Power Electronics,* vol. 38, no. 2, pp. 1622–1634, Feb. 2023.

[10] U. M. Choi, F. Blaabjerg, and K. B. Lee, "Control strategy of two capacitor voltages for separate MPPTs in photovoltaic systems using neutral-point-clamped inverters," in *IEEE Transactions on Industry Applications,* vol. 51, no. 4, pp. 3295–3303, Jul.-Aug. 2015.

[11] C. Qin and X. Li, "Improved virtual space vector modulation scheme for the reduced switch count three-level inverter with balanced and unbalanced neutral-point voltage conditions," in *IEEE Transactions on Power Electronics,* vol. 38, no. 2, pp. 2092–2104, Feb. 2023.

[12] Y. Park, S.-K. Sul, C.-H. Lim, and S.-H. Lee, "Asymmetric control of DC-link voltages for separate MPPTs in three-level inverters," in *IEEE Transactions on Power Electronics,* vol. 28, no. 6, pp. 2760–2769, Jun. 2013.

[13] Z. Zhang, A. Chen, X. Xing, and C. Zhang, "Space vector modulation based control strategy of three-level inverter for separate MPPTs in photovoltaic system," in *Proceedings of IEEE 8th International Power Electronics and Motion Control Conference,* 2016, pp. 2394–2400.

[14] Z. Ye, Y. Xu, X. Wu, G. Tan, X. Deng, and Z. Wang, "A simplified PWM strategy for a neutral-point-clamped (NPC) three-level converter with unbalanced dc links," in *IEEE Transactions on Power Electronics,* vol. 31, no. 4, pp. 3227–3238, Apr. 2016.

[15] X. Wu, G. Tan, Z. Ye, G. Yao, Z. Liu, and G. Liu, "Virtual-space-vector PWM for a three-level neutral-point-clamped inverter with unbalanced dc-links," in *IEEE Transactions on Power Electronics,* vol. 33, no. 3, pp. 2630–2642, Mar. 2018.

[16] X. Wu, G. Tan, G. Yao, C. Sun, and G. Liu, "A hybrid PWM strategy for three-level inverter with unbalanced dc links," in *IEEE Journal of Emerging and Selected Topics in Power Electronics,* vol. 6, no. 1, pp. 1–15, Mar. 2017.

[17] M. M. Hashempour, M. Yang, and T. Lee, "An adaptive control of DPWM for clamped-three-level photovoltaic inverters with unbalanced neutral-point voltage," in *IEEE Transactions on Industry Applications,* vol. 54, no. 6, pp. 6133–6148, Nov.-Dec. 2018.

[18] P. Zhang, X. Wu, B. Li, Li Ding, J. Long, W. Zhang, and Y. Li, "A zero-sequence component injection PWM scheme for three-level neutral point clamped rectifiers with unbalanced dc-link voltages," in *IEEE Transactions on Industrial Electronics,* vol. 12, no. 3, pp. 5420–5430, Jun. 2024.

[19] Y. Zou, L. Zhang, Y. Xing, H. Zhuge, X. Shen, Y. Zhang, and Y. Lu, "An optimized DPWM with reduced leakage current for three-phase three-level inverters with unbalanced neutral-point voltage," in *IEEE Transactions Power Electronics,* vol. 12, no. 3, pp. 16346–16360, Dec. 2024.

[20] C. Qin, X. Li, X. Xing, C. Zhang, and G. Zhang, "Common-mode voltage reduction method for three-level inverter with unbalanced neutral-point voltage conditions," in *IEEE Transactions on Industrial Informatics,* vol. 17, no. 10, pp. 6603–6613, Oct. 2021.

[21] M. Jing, C. Du, X. Xing, Z. Chen, and C. Wen, "The switching decomposition pulse width modulation with reduced common mode voltage for reduced switch counts neutral point clamped inverter," in *IET Power Electronics,* vol. 16, no. 4, pp. 612–630, Nov. 2022.

[22] M. C. Cavalcanti, K. C. de Oliveira, A M. de Farias, F. A. S. Neves, G. M. S. Azevedo, and F. C. Camboim, "Modulation techniques to eliminate leakage currents in transformerless three-phase photovoltaic systems," in *IEEE Transactions on Industrial Electronics,* vol. 57, no. 4, pp. 1360–1368, Apr. 2010.

[23] J. S. Lee and K. B. Lee, "New modulation techniques for a leakage current reduction and a neutral-point voltage balance in transformerless photovoltaic systems using a three-level inverter," in *IEEE Transactions on Power Electronics,* vol. 29, no. 4, pp. 1720–1732, Apr. 2014.

[24] C. Qin, C. Zhang, X. Xing, X. Li, A. Chen, and G. Zhang, "Simultaneous common-mode voltage reduction and neutral-point voltage balance scheme for the quasi-Z-source three-level T-type inverter," in *IEEE Transactions on Industrial Electronics,* vol. 67, no. 3, pp. 1956–1967, Mar. 2020.

[25] Y. Huang, T. Liu, Q. Ren, A. Chen, H. Zhang, and W. Wang, "Data-driven predictive control strategy to improve robust performance for three-level inverters with reduced common-mode voltage," in *IEEE Journal of Emerging and Selected Topics in Power Electronics,* vol. 12, no. 4, pp. 3823–3834, Aug. 2024.

[26] K. Nanshikar and S. Das, "Optimal space vector-based hybrid PWM scheme in terms of common-mode voltage and line current ripple," in *IEEE Transactions on Power Electronics,* vol. 39, no. 11, pp. 14478–17792, Nov. 2024.

[27] X. Tang, X. Yuan, S. Niu, and K. T. Chau, "High-efficient multivector model predictive control with common-mode voltage suppression," in *IEEE Journal of Emerging and Selected Topics in Power Electronics,* vol. 12, no. 3, pp. 2674–2885, Jun. 2024.

[28] Q. Yan, H. Chen, T. Zhao, X. Yuan, L. Zhang, and R. Zhao, "A carrier-based discontinuous space-vector PWM for common-mode voltage reduction in dual-input three-level T-type inverters with unbalanced neutral-point voltages," in *IEEE Transactions on Power Electronics,* vol. 39, no. 9, pp. 11020–11033, Feb. 2024.

[29] Z. Li, X. Xing, C. Liu, C. Wen, and R. Zhang, "Common-mode voltage reduction method-based flexible power control for multiport DC-AC converter in PV-battery hybrid system," in *IEEE Journal of Emerging and Selected Topics in Power Electronics,* vol. 12, no. 3, pp. 2744–2757, Jun. 2024.

[30] X. Li, C. Qin, Z. Chu, and J. Fang, "A novel modulation scheme for simultaneous common-mode voltage reduction and neutral-point voltage balance in the reduced switch count quasi-Z-source three-level inverter," in *IEEE Transactions on Power Electronics,* vol. 38, no. 10, pp. 12035–12047, Oct. 2023.

[31] X. Pang, A. Chen, X. Li, Z. Zhong, and X. Liu, "Carrier-based fault tolerant control strategies for three-level T-type inverter with unbalanced neutral-point voltage," in *IEEE Journal of Emerging and Selected Topics in Power Electronics,* vol. 12, no. 4, pp. 4154–4164, Aug. 2024.

**Zhiyuan Chu** received the B.S. degree in building electricity and intelligence in 2022 from Shandong Jianzhu University, Jinan, China, where he is currently working toward the M.S. degree in control engineering. His current research interests include modulation strategies of multi-level converters.

**Changwei Qin** received the Ph.D. degree in electrical engineering from Shandong University, Jinan, China, in 2019. In 2020, he joined Shandong Jianzhu University, where he is currently an Associate Professor. His current research interests include control of multi-level converters and impedance source converters.

**Xiaoyan Li** received the Ph.D. degree in electrical engineering from Shandong University, Jinan, China, in 2020. From 2021 to 2023, she was a Postdoctoral Research Fellow with Shandong University, Jinan, China. In 2023, she joined Shandong Jianzhu University, where she is currently a Full Professor. Her current research interests include control of multi-level converters and power quality control.

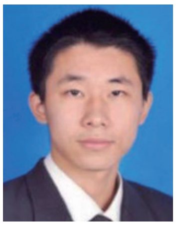

**Jingyang Fang** received the B.Sc. and M.Sc. degrees in electrical engineering from Xi'an Jiaotong University, Xi'an, China, in 2013 and 2015, respectively, and the Ph.D. degree from the School of Electrical and Electronic Engineering, Nanyang Technological University, Singapore, in 2019.

From May 2018 to August 2018, he was a Visiting Scholar with the Institute of Energy Technology, Aalborg University, Aalborg, Denmark. From August 2018 to August 2019, he was a Research Fellow with School of Electrical and Electronic Engineering, Nanyang Technological University, Singapore. From August 2019 to August 2021, he was a Postdoctoral Researcher with the Duke University and TU Kaiserslautern. Since August 2021, he has joined School of Control Science and Engineering, Shandong University as a Full Professor. His research interests include power quality control, stability analysis and improvement, renewable energy integration, and digital control in more-electronics power systems.

Dr. Fang is a recipient of the Humboldt Research Fellowship, two IEEE Prize Paper Awards, one Best Presenter Award, and the IEEE JESTPE Star Reviewer Award. He received the Chinese Government Award for Outstanding Self-Financed Students Abroad in 2018 and the Best Thesis Award from NTU in 2019. He was World's Top 2% Highly Cited Scientists ranked by Stanford University.

**Lei Yang** received the B.S. degree in electrical engineering and automation in 2023 from Shandong Jianzhu University, Jinan, China, where he is currently working toward the M.S. degree in control science and engineering. His current research interests include modulation strategies of multi-level converters.

**Yanling Zhang** received the M.S. degree in control science and engineering from Northeastern University, Shenyang, China, in 2009. She is currently an experimentalist with the School of Information and Electrical Engineering, Shandong Jianzhu University. Her research interests include embedded system design.